SUPPLEMENTARY METHODS

Sedimentological and geochemical methods

Core LN2

Physical properties (magnetic susceptibility, wet bulk density) were measured on whole cores using a Geotek multi-sensor core logger at the British Ocean Sediment Core Research Facility (BOSCORF) at the National Oceanography Centre, Southampton, UK. Core LN2 was split, described and sub-sampled at the British Antarctic Survey (BAS) in Cambridge, UK. The split core halves were X-rayed at the Department of Veterinary Medicine, University of Cambridge, UK. Diatom content was assessed qualitatively from sediment smear slides. Individual sediment sub-samples (1-cm-thick slices) were then taken every 2–5 cm and used to determine water content, grain size and total organic carbon (TOC). TOC was determined using a Vario EL III Elemental analyser at the Institute for Geophysics and Geology, University of Leipzig, Germany. Analytical precision was 1% for the total-carbon measurements and 3% for the TOC measurements. Proportions of gravel (>2 mm), sand (63 μm to 2 mm), and mud (<63 μm) were determined on a weight basis by wet sieving. Gravel grains (>2–8 mm) and pebbles (>8 mm) were also counted on the X-radiographs at 1-cm depth intervals. All coarse fraction (>63 μm) samples (n = 37) were inspected under a light microscope for any microfossils. Samples were not pre-treated before or after sieving. An aliquot of the ≤2-μm fraction was used to determine the relative contents of the clay minerals smectite, illite, chlorite and kaolinite using an automated powder x-ray diffractometer system (Rigaku MiniFlex) with CoKα radiation (30 kV, 15 mA) at the Institute for Geophysics and Geology, University of Leipzig, Germany. The clay mineral identification and quantification followed standard methods (Ehrmann et al., 2011). X-ray fluorescence (XRF) measurements were carried out every 0.5 cm using an Avaatech XRF-Core Scanner at the Godwin Laboratory for Palaeoclimate Research, Department of Earth Sciences, University of Cambridge, UK. Data were evaluated by analysis of the X-ray spectra generated at each energy level using the WIN AXIL Batch software (www.canberra.com). XRF data are presented as area counts per second.

Core VC331

Laboratory methods, sedimentological results and interpretation of core VC331 can be found in Curry and Pudsey (2007).

Core chronology

Core LN2

Multiple-dating methods were applied to core LN2. However, owing to complex radiocarbon data the chronology for core LN2 is based primarily on data representing variations in the relative paleointensity (RPI) of the Earth's magnetic field, which can be estimated from the natural remanent magnetization (NRM) of marine sediments. Samples for rock and paleomagnetic measurements were taken continuously down core using 2.2 cm x 2.2 cm x 1.8 cm plastic cubes resulting in a depth resolution of ~2.3 cm. Measurements were undertaken at the Paleomagnetic Laboratory at the Faculty of Geosciences, University of Bremen, Germany. Directions and intensities of NRM were measured on a superconducting rock magnetometer (2G Enterprises model 755 HR). NRM was determined on each sample before it was subjected to a systematic demagnetization treatment involving 15 steps for each sample applying 5 mT increments up to an alternating field of 50 mT and 10 mT increments in alternating fields between 60 and 100 mT. A detailed vector analysis was applied to the results (Kirschvink, 1980) in order to determine the characteristic remanent magnetization (ChRM). Anhysteretic remanent magnetization (ARM) was imparted on the samples in a peak alternating field of 100 mT in presence of a biasing steady field of 50 μT, while isothermal remanent magnetization (IRM) was stepwise acquired in DC fields up to 700 mT in-line on the same instrument. ARM and IRM were AF demagnetized applying the same peak fields as for demagnetization of the NRM. Paleointensity estimates in sediments are established by dividing (normalizing) NRM intensity by a magnetic parameter reflecting the variable amount of magnetic particles. Such parameters can be magnetic susceptibility (κ), ARM and IRM. Magnetic susceptibility is usually rejected as it is affected by large magnetite grains (often present in sediments containing in ice-rafted debris) and very fine particles, both of which do not significantly contribute to magnetic remanence (Channell et al., 2002). RPI was computed using the so-called `slope-method' or pseudo Thellier method (Channell et al., 2002; Tauxe et al., 1995). It was calculated as the slope of the regression line of NRM intensities plotted versus the intensities of ARM for alternating field demagnetization levels from 35 to 50 mT. RPI data are always shown in standardized form (mean subtracted and divided by standard deviation).

Homogeneity in terms of concentration, grain size and mineralogy of the magnetic mineral assemblage is considered a measure for the goodness of the RPI estimate. The concentration of magnetic particles, reflected by ARM, IRM, and magnetic susceptibility (κ), should not vary by more than a factor of 10 (King et al., 1983; Tauxe et al., 1995). For core LN2, all three

normalizers, ARM, IRM, and magnetic susceptibility (κ) vary downcore by a factor of less than 6 (Table DR1, Fig. DR1). Plotting anhysteretic susceptibility (κ_{ARM}), i.e., ARM divided by the biasing DC field, versus magnetic susceptibility (κ) provides an opportunity to examine magnetic grain size (King et al., 1983). Values for magnetic susceptibility (κ) were transferred from whole core measurements by interpolation to the respective depths of the discrete samples. The data for core LN2 plot in a relatively narrow area indicating small and relatively uniform particle sizes (Fig. DR2). Three samples from the uppermost ~10 cm plot outside this narrow area. They originate from a core interval with slightly changing magnetic mineralogy as indicated by the pseudo s-ratio IRM_{300mT}/IRM_{700mT} computed following (Stoner and St-Onge, 2007). Although the numbers of the pseudo s-ratio are different from the classical S-ratio (Bloemendal et al., 1992), the information provided is similar. A ratio of 1 indicates that the magnetic mineral assemblage consists of only low-coercivity minerals as e.g. magnetite with enhanced magnetic susceptibility. Decreasing ratios indicate increasing proportions of high-coercivity minerals as e.g. hematite. For core LN2 we find a relative increase of low-coercivity minerals from ~30 cm core depth upward. The coinciding slight up-core coarsening of the magnetic particles (indicated by decreasing κ_{ARM}/κ ratios) likely contributes to the increase in magnetic susceptibility towards the core top (Fig. DR1).

The RPI estimates for all three normalizers (ARM, IRM, κ) show very similar results, although the relative amplitudes of minima and maxima differ between the normalizers (Fig. DR1). Ideal normalizers show no coherence with the normalized NRM intensity. Thus, coherency was evaluated by applying the program SPECTRUM (Schulz and Stattegger, 1997) to the RPI data for core LN2. LN2 RPI is not coherent at the 95% significance level for all three normalizers (Fig. DR3) except for periods of 129 and 137 yr for susceptibility and 205 and 207 yr for ARM and IRM, respectively. We chose ARM as normalizer because its coherence with normalized NRM intensity is the weakest. Furthermore, the intensities of ARM and NRM are in the same order, whereas IRM intensity is several hundreds of times larger than NRM intensity. Additionally, ARM typically reflects a similar coercivity range as NRM because the ratio of NRM to ARM is often quite stable over a broad range of demagnetization steps (Tauxe et al., 1995), whereas the ratio of NRM to IRM is unstable.

RPI for core LN2 is tuned to a RPI record from the western Bransfield Basin (WBB), west of the AP (hereafter referred to as the WBB RPI stack) (Willmott et al., 2006). Correlation of LN2

RPI to the WBB RPI stack (Fig. DR4) yields a correlation coefficient (Pearson's 'r') of r = 0.88 when linearly interpolating both data sets on an increment of 60 years resulting in 109 data pairs. The WBB RPI stack was not independently dated. Willmott et al. (2006) used a 2-step tuning process to derive their age model. They tuned the WBB RPI stack first to an absolute paleointensity compilation termed ABSINT (Laj et al., 2002; Yang et al., 2000) and then to a high-resolution RPI record from the St. Lawrence Estuary, which had been dated by AMS^{14}C chronology (St-Onge et al., 2003). Therefore, accuracy of the age model for core LN2 is limited to that of the tuning target WBB RPI stack. For the past ~500 years (i.e. the upper ~30 cm of the core), the LN2 RPI record shows increased intensities diverging from the ABSINT curve and also from direct observations by geomagnetic observatories. This likely relates to the aforementioned change in magnetic mineralogy and/or a minor coarsening of magnetic grains. The ratio of soft magnetic minerals to hard magnetic minerals is almost constant until 500 yr, i.e. 30 cm core depth, but increased in more recent times (Fig. DR1). Apparently, ARM does not sufficiently account for this and thus also not NRM normalization by ARM. Although we consider the LN2 RPI less meaningful for the last 500 yr, the developed LN2 age model is not at all affected because no tie point originates from this time interval. Despite its limitations, we regard the RPI data-based age model for core LN2 as sufficiently accurate to provide sound chronological constraints.

^{210}Pb and ^{137}Cs activity were measured on 0.5 cm-thick sediment slices by way of gamma spectrometry using Canberra ultra-low-background germanium detectors at the Gamma Dating Centre, Department of Geosciences and Natural Resource Management, University of Copenhagen, Denmark (Fig. DR5). ^{210}Pb was measured by way of its gamma peak at 46.5 keV, ^{226}Ra by way of its granddaughter ^{214}Pb (peaks at 295 keV and 352 keV), and ^{137}Cs by way of its peak at 661 keV. Unsupported ^{210}Pb is ~20 Bq kg−1 in the surface sediments. Below 12 cm, ^{210}Pb activity was at or below detection limits. ^{137}Cs was largely below detection limits throughout, although this is relatively common in Antarctic glacimarine environments due to the low fallout in the Southern Hemisphere and its natural decay since deposition (Smith et al., 2019). Importantly, the activity of excess ^{210}Pb in the surface sediments indicates modern (younger than ~150 years) deposition. The lack of a typical decay profile likely reflects (1) enhanced bioturbation, which is clearly visible in the X-radiographs (Fig. 2C), or (2) higher sedimentation rates, or a combination of both. Whilst it is not possible to calculate an age-model from the ^{210}Pb data because of the lack of exponential decay with depth, we point out that the RPI age-model appears to provide a reasonable approximation (12 cm = ~180 yr).

The mini radiocarbon dating system (MICADAS) was used to date low-mass calcareous microfossil samples (obtained from the uppermost 12 cm in core LN2) at the Accelerator Mass Spectrometry (AMS) radiocarbon dating facility at the Swiss Federal Institute of Technology (ETH) in Zűrich, Switzerland (Wacker et al., 2010). The dated samples display a narrow age-range (7,520-9,838 ^{14}C yr B.P.; Table DR2) but are incompatible with ^{210}Pb data which indicate 'modern' seafloor surface sediments. However, because such organisms cannot survive in a subglacial environment they must have colonized the sea-floor after grounding line retreat. We argue that the predominantly benthic (micro-)fossils were incorporated into the ice shelf by basal freeze-on, similar to what has been observed for the modern McMurdo Ice Shelf (Hall et al., 2010; Kellogg and Truesdale, 1979), and that these fossils have only recently melted out. As such, we use this oldest age as a minimum age-constraint for the transition from subglacial to glacimarine sedimentation on the inner shelf. Small numbers of planktic foraminifera tests (n = 20) are likely to have been advected beneath the ice shelf from the open ocean.

AMS ^{14}C dating of the 'bulk' AIO fraction in core LN2 was performed at Beta Analytic Inc., Florida, U.S.A. The AIO dates yielded consistently old ages (14,400-25,900 ^{14}C yr B.P.), with a core top age of 25,900 ^{14}C yr B.P. These anomalously old ages are consistent with previous work on the eastern AP shelf (Pudsey et al., 2006; Rebesco et al., 2014) and indicate that marine sediment in this region is significantly influenced by the ad-mixture of fossil organic carbon (Table DR2). This is likely derived from the organic-rich sedimentary strata, such as the Trinity Peninsula formation and Botany Bay group. To help mitigate the effects of recycled fossil carbon we applied Ramped PyrOx ^{14}C dating (Subt et al., 2017). All samples were prepared at the College of Marine Science, University of South Florida and analysed at the National Ocean Sciences Accelerator Mass Spectrometry (NOSAMS) facility for ^{14}C/^{12}C ratio determination. The horizons which yielded the oldest AIO ^{14}C ages in core LN2 also resulted in erroneously old Ramped PyrOx ^{14}C ages that are incompatible with RPI and ^{210}Pb data (Fig. DR5, Table DR2). This indicates that the proportion of 'modern' carbon in most of the dated samples is too low, and even with ramped pyrolysis steps, the resulting age-data reflect the failure to separate autochthonous organic carbon from fossil carbon even at low pyrolysis temperatures. We suggest this problem is particularly acute in inner shelf areas that are underlain by and/or situated close to outcropping organic-rich sedimentary strata. This might explain, why samples from core VC331 yielded more reliable Ramped PyrOx ^{14}C ages (Table DR2).

Age-depth modelling of core LN2, using the RPI and ^{210}Pb tie-points (Fig. DR5), was undertaken with CLAM v2.233 using linear interpolation between neighbouring levels (Blaauw, 2010). Ages were calculated every 10 cm. Interpolated ages in the text are based on the 'best-fit' age from the CLAM age-depth model. The age-uncertainty is 0.25 kyr for the PRI ages, taken from the average uncertainty in the Wilmott et al. (2006) dataset. For Ramped PyrOx ^{14}C ages, the analytical error is given in the text (Table DR1).

Core VC331

The Ramped PyrOx ^{14}C method was also applied to organic matter samples from core VC331. Similar to core LN2, dating of the bulk AIO fraction revealed considerable contamination from fossil organic carbon, with ^{14}C ages ranging from 17,280 to 26,740 ^{14}C yr B.P. (Table DR3, Fig. DR6). Ramped PyrOx ^{14}C dates are consistently younger than the AIO ages (11,170-15,970 ^{14}C yr B.P.) and provide (minimum) constraints for the timing of grounding and calving line retreat from its more expanded Last Glacial Maximum position.

REFERENCES

Blaauw, M., 2010, Methods and code for 'classical' age-modelling of radiocarbon sequences: Quaternary Geochronology, v. 5, no. 5, p. 512-518.

Bloemendal, J., King, J. W., Hall, F. R., and Doh, S.-J., 1992, Rock magnetism of Late Neogene and Pleistocene deep-sea sediments: Relationship to sediment source, diagenetic processes, and sediment lithology: Journal of Geophysical Research: Solid Earth, v. 97, no. B4, p. 4361-4375.

Channell, J. E. T., Mazaud, A., Sullivan, P., Turner, S., and Raymo, M. E., 2002, Geomagnetic excursions and paleointensities in the Matuyama Chron at Ocean Drilling Program Sites 983 and 984 (Iceland Basin): Journal of Geophysical Research: Solid Earth, v. 107, no. B6, p. EPM 1-1-EPM 1-14.

Ehrmann, W., Hillenbrand, C.-D., Smith, J. A., Graham, A. G. C., Kuhn, G., and Larter, R. D., 2011, Provenance changes between recent and glacial-time sediments in the Amundsen Sea embayment, West Antarctica: clay mineral assemblage evidence: Antarctic Science, v. 23, no. 5, p. 471-486.

Hall, B. L., Henderson, G. M., Baroni, C., and Kellogg, T. B., 2010, Constant Holocene Southern-Ocean 14C reservoir ages and ice-shelf flow rates: Earth and Planetary Science Letters, v. 296, no. 1, p. 115-123.

Jung, J., Yoo, K.-C., Rosenheim, B. E., Conway, T. M., Lee, J. I., Yoon, H. I., Hwang, C. Y., Yang, K., Subt, C., and Kim, J., 2019, Microbial Fe(III) reduction as a potential iron source from Holocene sediments beneath Larsen Ice Shelf: Nature Communications, v. 10, no. 1, p. 5786.

Kellogg, T. B., and Truesdale, R. S., 1979, Late Quaternary paleoecology and paleoclimatology of the Ross Sea: the diatom record: Marine Micropaleontology, v. 4, p. 137-158.

King, J. W., Banerjee, S. K., and Marvin, J., 1983, A new rock-magnetic approach to selecting sediments for geomagnetic paleointensity studies: Application to paleointensity for the last 4000 years: Journal of Geophysical Research: Solid Earth, v. 88, no. B7, p. 5911-5921.

Kirschvink, J. L., 1980, The least-squares line and plane and the analysis of palaeomagnetic data: Geophysical Journal of the Royal Astronomical Society, v. 62, no. 3, p. 699-718.

Laj, C., Kissel, C., Mazaud, A., Michel, E., Muscheler, R., and Beer, J., 2002, Geomagnetic field intensity, North Atlantic Deep Water circulation and atmospheric Δ14C during the last 50 kyr: Earth and Planetary Science Letters, v. 200, no. 1, p. 177-190.

Ó Cofaigh, C., Davies, B. J., Livingstone, S. J., Smith, J. A., Johnson, J. S., Hocking, E. P., Hodgson, D. A., Anderson, J. B., Bentley, M. J., Canals, M., Domack, E., Dowdeswell, J. A., Evans, J., Glasser, N. F., Hillenbrand, C.-D., Larter, R. D., Roberts, S. J., and Simms, A. R., 2014, Reconstruction of ice-sheet changes in the Antarctic Peninsula since the Last Glacial Maximum: Quaternary Science Reviews, v. 100, no. 0, p. 87-110.

Pudsey, C. J., Murray, J. W., Appleby, P., and Evans, J., 2006, Ice shelf history from petrographic and foraminiferal evidence, Northeast Antarctic Peninsula: Quaternary Science Reviews, v. 25, no. 17-18, p. 2357-2379.

Rebesco, M., Domack, E., Zgur, F., Lavoie, C., Leventer, A., Brachfeld, S., Willmott, V., Halverson, G., Truffer, M., Scambos, T., Smith, J., and Pettit, E., 2014, Boundary condition of grounding lines prior to collapse, Larsen-B Ice Shelf, Antarctica: Science, v. 345, no. 6202, p. 1354-1358.

Schulz, M., and Stattegger, K., 1997, Spectrum: spectral analysis of unevenly spaced paleoclimatic time series: Computers & Geosciences, v. 23, no. 9, p. 929-945.

Smith, J. A., Graham, A. G. C., Post, A. L., Hillenbrand, C. D., Bart, P. J., and Powell, R. D., 2019, The marine geological imprint of Antarctic ice shelves: Nature Communications, v. 10.

St-Onge, G., Stoner, J. S., and Hillaire-Marcel, C., 2003, Holocene paleomagnetic records from the St. Lawrence Estuary, eastern Canada: centennial- to millennial-scale geomagnetic modulation of cosmogenic isotopes: Earth and Planetary Science Letters, v. 209, no. 1, p. 113-130.

Stoner, J., and St-Onge, G., 2007, Chapter Three Magnetic Stratigraphy in Paleoceanography: Reversals, Excursions, Paleointensity, and Secular Variation: Developments in Marine Geology, v. 1.

Subt, C., Yoon, H. I., Yoo, K. C., Lee, J. I., Leventer, A., Domack, E. W., and Rosenheim, B. E., 2017, Sub-ice shelf sediment geochronology utilizing novel radiocarbon methodology for highly detrital sediments: Geochemistry Geophysics Geosystems, v. 18, no. 4, p. 1404-1418.

Tauxe, L., Pick, T., and Kok, Y. S., 1995, Relative paleointensity in sediments: A Pseudo-Thellier Approach: Geophysical Research Letters, v. 22, no. 21, p. 2885-2888.

Wacker, L., Bonani, G., Friedrich, M., Hajdas, I., Kromer, B., Nemec, M., Ruff, M., Suter, M., Synal, H. A., and Vockenhuber, C., 2010, MICADAS: Routine and High-Precision Radiocarbon Dating: Radiocarbon, v. 52, no. 2, p. 252-262.

Willmott, V., Domack, E. W., Canals, M., and Brachfeld, S., 2006, A high resolution relative paleointensity record from the Gerlache-Boyd paleo-ice stream region, northern Antarctic Peninsula: Quaternary Research, v. 66, no. 1, p. 1-11.

Yang, S., Odah, H., and Shaw, J., 2000, Variations in the geomagnetic dipole moment over the last 12 000 years: Geophysical Journal International, v. 140, no. 1, p. 158-162.

FIGURE AND TABLE CAPTIONS

Figure DR1. Rock and paleomagnetic parameters, together with sedimentological parameters for core LN2 plotted against depth. From left to right: NRM intensity, ARM and IRM intensities as proxies for magnetic mineral concentration, magnetic susceptibility (κ), relative paleointensity (RPI) normalized by ARM (blue), IRM (black) and magnetic susceptibility (red) with all RPI data shown in standardized form (mean subtracted and divided by standard deviation) pseudo s-ratio IRM_{300mT}/IRM_{700mT} as crude estimate for the ratio of soft to hard magnetic minerals, κ_{ARM}/κ as magnetic grain size proxy, inclination of characteristic remanent

magnetization Inc_{ChRM} and percentages of bulk sediment with grain size fractions 63 μm, 2 mm and >2mm, respectively.

Figure DR2. Anhysteretic susceptibility κ_{ARM} plotted against magnetic susceptibility (κ) as proxy for magnetic grain size and concentration (King et al., 1983).

Figure DR3. Squared coherence of normalized NRM intensity with normalization parameters ARM, IRM, and magnetic susceptibility, respectively, for LN2 (thin lines). The dashed horizontal line is the level above which squared coherence is considered significant at the 95% level. Power spectra of RPI_{ARM} for core LN2 (thick black line).

Figure DR4. A: Relative paleointensity record (LN2 RPI) for core LN2 (red curve) tuned to the WBB RPI stack (Willmott et al., 2006) from west of the Antarctic Peninsula (black curve); LN2 RPI shown in standardized form (mean subtracted and divided by standard deviation). LN2 RPI data for the last 500 yr are plotted as dotted line to account for larger uncertainty in that interval. RPI tie points are shown as dashed lines. LN2 RPI data are constrained by ^{210}Pb data indicating a modern surface age. **B:** Output ages for LN2 RPI and ^{210}Pb tie points. **C**: Age-depth plot of RPI and ^{210}Pb-derived tie-points.

Figure DR5. A: ^{14}C age-depth plot for core LN2. The erroneously old acid insoluble organic matter (AIO) and Ramped PyrOx (RP) ^{14}C ages reflect input of fossil carbon. **B:** ^{210}Pb and ^{137}Cs activity as a function of depth for core LN2. Error bars denote one standard deviation of ^{210}Pb and ^{137}Cs concentrations. Note that the concentration of ^{137}Cs is at or below the detection limit for the majority of samples. The high concentrations of $^{210}Pb_{xs}$ indicate that the surface of core LN2 is modern. $^{210}Pb_{xs}$ = excess ^{210}Pb.

Figure DR6. ^{14}C age-depth plot for core VC331 showing acid insoluble organic matter (AIO) and Ramped PyrOx (RP) ^{14}C age data. Composite RP age is thought to represent the true age of the sample.

Figure DR7. Simplified core lithology and Ramped PyrOx ^{14}C ages (cal. kyr B.P.) for core GC16-B (adapted from Subt et al., 2017 and (Jung et al., 2019)).

Table DR1. First column: Coefficient of determination r^2 for LN2 RPI and rock magnetic parameters ARM and IRM intensities, magnetic susceptibility (κ) and magnetic grain size proxy κ_{ARM}/κ. and sediment grain size fractions <63 μm, 63 μm-2 mm, and >2 mm, respectively. Lowermost numbers show r^2 computed for core sub-sections as indicated. **Second column**: r^2 for ARM intensity and respective rock magnetic and sedimentological parameters. **Third column**: r^2 for inclination of characteristic remanent magnetization $Incl._{ChRM}$ and respective rock magnetic and sedimentological parameters. **Fourth column**: Ratio of maximum to minimum value of respective rock magnetic parameter.

Table DR2. Compilation of radiocarbon ages for cores LN2 and VC331, showing material dated and method. Pf = planktic foraminifera, bf = benthic, bryo = bryozoans, gp = gastropod

shell. AIO = acid insoluble organic matter, MICADAS = mini carbon dating system. All ^{14}C-ages were corrected using a marine reservoir effect (MRE) of 1230±100 (ΔR of 830 ± 100 years) (Ó Cofaigh et al., 2014). Corrected ^{14}C-ages were calibrated with the CALIB Radiocarbon Calibration Program version 7.0.4 (http://calib.qub.ac.uk/calib/) using the MARINE09 calibration dataset. Errors of calibrated dates are given as a 2σ range (min, max and mean). Ages used in our ice sheet reconstruction are shaded grey.

Table DR3. Ramped PyrOx AMS ^{14}C data for LN2 and VC331, including core, sample depth, CO_2 split (or aliquot) number, temperature interval over which the CO_2 split was obtained (°C), δ^{13}C (per mil), fraction modern and reported age (^{14}C yr BP). Fraction modern (fm) and ages are black corrected using in-house methods. Grey shading indicates the composite age, thought to represent the true age of the sample (see Subt et al., 2017).

Figure DR1.

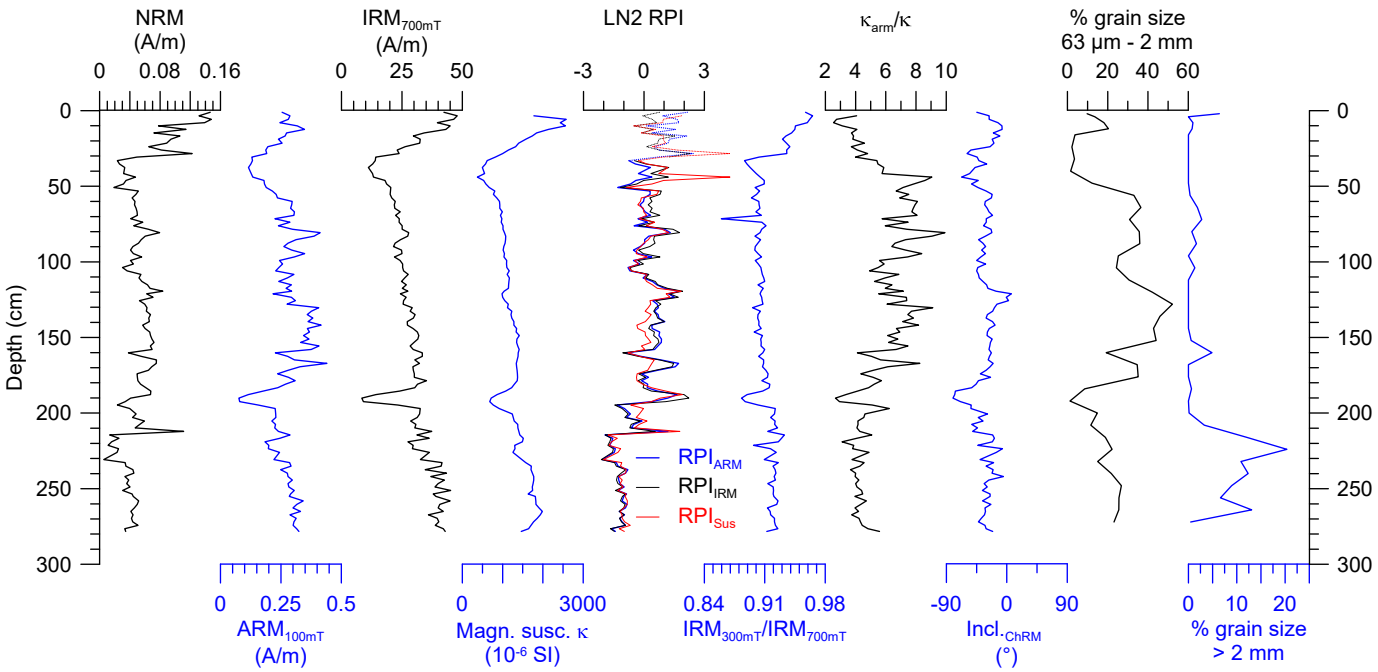
NRM
(A/m)
0 0.08 0.16
IRM700mT
(A/m)
0 25 50
LN2 RPI
-3 0 3
κarm/κ
2 4 6 8 10
% grain size
63 µm - 2 mm
0 20 40 60
Depth (cm)
0 50 100 150 200 250 300
RPIARM
RPIIRM
RPISus
0 0.25 0.5
ARM100mT
(A/m)
0 3000
Magn. susc. κ
(10-6 SI)
0.84 0.91 0.98
IRM300mT/IRM700mT
-90 0 90
Incl.ChRM
(°)
0 10 20
% grain size
> 2 mm

Figure DR2.

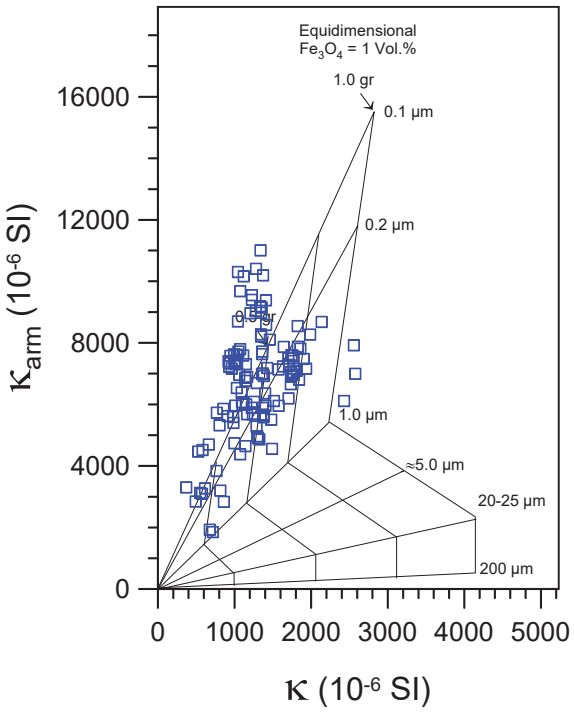
Equidimensional
Fe3O4 = 1 Vol.%
1.0 gr
0.1 µm
0.2 µm
1.0 µm
≈5.0 µm
20-25 µm
200 µm
16000
12000
8000
4000
0
0
1000
2000
3000
4000
5000
κarm (10-6 SI)
κ (10-6 SI)

Figure DR3.

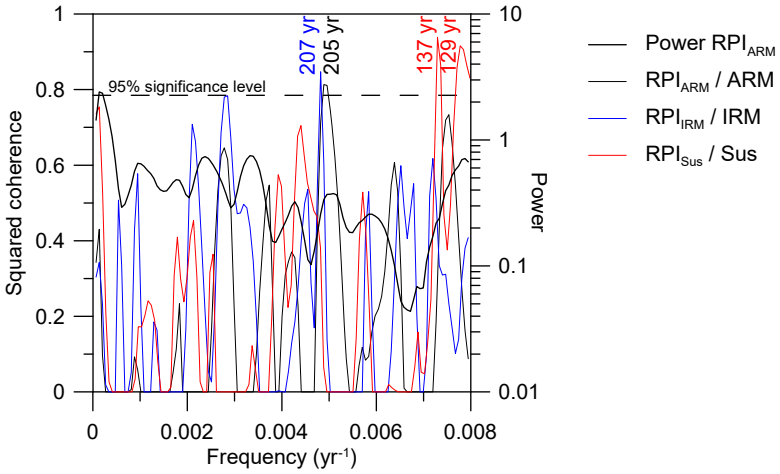
Squared coherence
Power
Frequency (yr⁻¹)
95% significance level
207 yr
205 yr
137 yr
129 yr
Power RPI_ARM
RPI_ARM / ARM
RPI_IRM / IRM
RPI_Sus / Sus

Figure DR4.

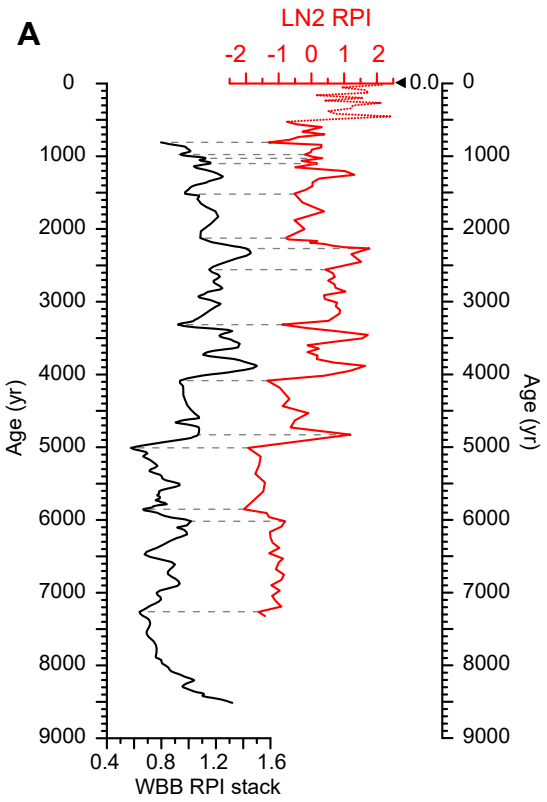

B

Depth (cm)	Age (yr)	Dating method
0	0	^{210}Pb
50.8	809	RPI
62.3	976	RPI
69.2	1027	RPI
73.8	1100	RPI
92.2	1514	RPI
103.7	2123	RPI
119.4	2268	RPI
125.7	2558	RPI
160.2	3314	RPI
187.8	3882	RPI
194.7	4084	RPI
212.1	4827	RPI
214.4	5009	RPI
230.7	5852	RPI
237.4	6018	RPI
276.5	7263	RPI

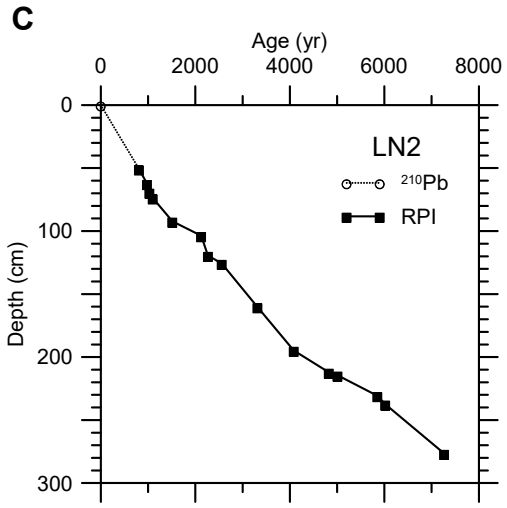

Figure DR5.

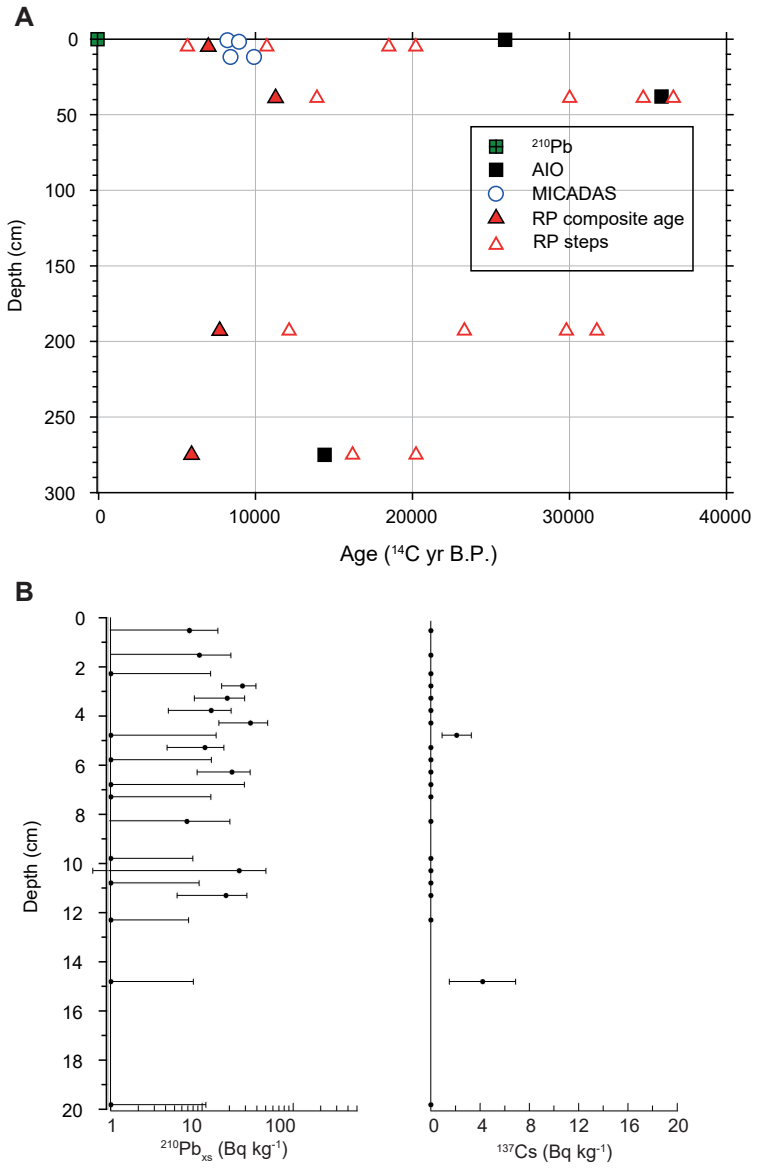
A
Depth (cm)
Age (14C yr B.P.)
210Pb
AIO
MICADAS
RP composite age
RP steps
B
Depth (cm)
210Pbxs (Bq kg-1)
137Cs (Bq kg-1)

Figure DR6.

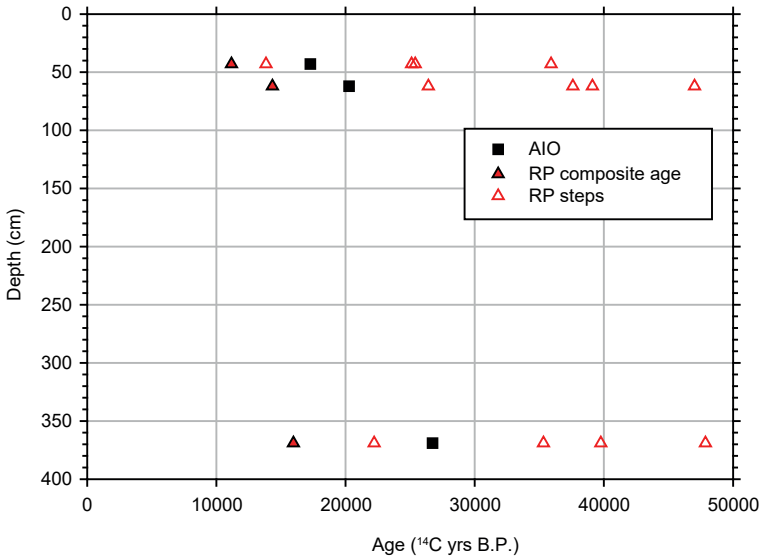
0
50
100
150
200
250
300
350
400
Depth (cm)
0
10000
20000
30000
40000
50000
Age (14C yrs B.P.)
AIO
RP composite age
RP steps

Figure DR7.

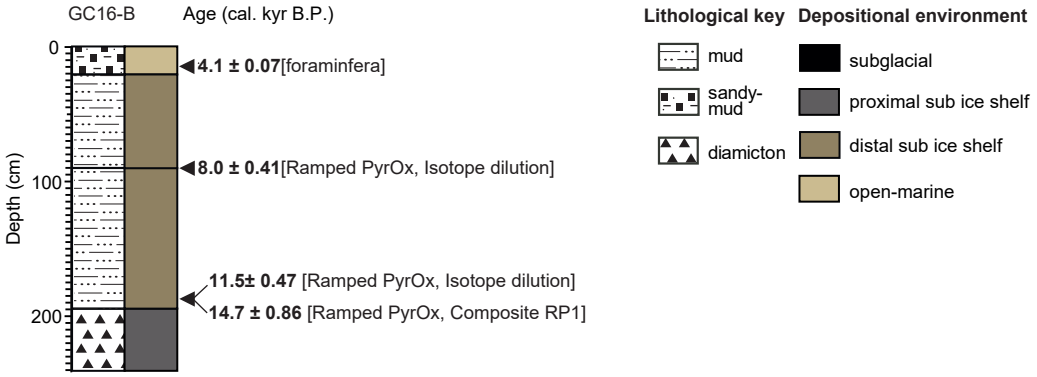
GC16-B
Age (cal. kyr B.P.)
Depth (cm)
0
100
200
4.1 ± 0.07[foraminfera]
8.0 ± 0.41[Ramped PyrOx, Isotope dilution]
11.5± 0.47 [Ramped PyrOx, Isotope dilution]
14.7 ± 0.86 [Ramped PyrOx, Composite RP1]
Lithological key
mud
sandy-mud
diamicton
Depositional environment
subglacial
proximal sub ice shelf
distal sub ice shelf
open-marine

Table DR1.

r^2	RPI	ARM intensity	$Incl._{ChRM}$	Max/Min
NRM intensity	0.676	0.064	0.020	27.6
ARM intensity	0.017	n.a.	0.295	5.8
IRM intensity	0.055	0.266	0.166	5.7
Magnetic suscepibility κ	0.015	0.188	0.171	5.7
κ_{arm}/κ	0.060	0.188	0.013	3.9
<63 µm	0.005	0.477	0.308	
63 µm - 2 mm	0.022	0.513	0.252	
>2 mm (2.1 - 278.3 cm)	0.390	0.000	0.037	
>2 mm (2.1 - 209.8 cm)	0.083			
>2 mm (212.1 - 278.3 cm)	0.047			

Lab code	Core	Depth (cm)	Material dated	Method	14C age	error	MRE	Cal. yr B.P. 2s min	2s max	2s mean
370532	LN2	0-1	Organic sediment	AIO	25900	130	1230	-	-	-
370533	LN2	38	Organic sediment	AIO	35860	400	1230	-	-	-
370534	LN2	275	Organic sediment	AIO	14400	70	1230			
59751.1.1	LN2	1	Mixed pf, bf	MICADAS	8225	145	1230	7520	8209	**7865**
59752.1.1	LN2	2	bryo	MICADAS	8955	175	1230	8174	9150	**8662**
59753.1.1	LN2	12	gp	MICADAS	9915	85	1230	9514	10161	**9838**
59756.1.1	LN2	12	bryo	MICADAS	8420	75	1230	7807	8321	**8064**
DB1599,1616,17,19,20,22-RP1	LN2	5	Organic sediment	Ramped Pyrox	6990	330	1230	6514	7915	**7215**
DB160-0,1,3,4,5,6,7,8,9 RP1	LN2	39	Organic sediment	Ramped Pyrox	11280	810	1230	9513	13466	**11490**
DB1595,1611,12,14,39-RP1	LN2	193	Organic sediment	Ramped Pyrox	7720	270	1230	6755	7935	**7345**
DB1598, 1625, 1626-RP1	LN2	275	Organic sediment	Ramped Pyrox	5920	140	1230	5140	5696	**5418**
DB1633-1	VC331	43	Organic sediment	Ramped Pyrox	11170	160	1230	10905	12128	**11517**
DB1634-1	VC331	62	Organic sediment	Ramped Pyrox	14340	240	1230	14855	16501	**15678**
DB1651-1	VC331	369	Organic sediment	Ramped Pyrox	15970	530	1230	16402	19073	**17738**
470169	VC331	43	Organic sediment	AIO	17280	50	1230	-	-	-
470170	VC331	62	Organic sediment	AIO	20280	80	1230	-	-	-
470171	VC331	369	Organic sediment	AIO	26740	110	1230	-	-	-

Table DR2

Sample ID	Fm	Fm error	d13C	umol CO2	mg CO2	#runs	14C Age	error
DB1599,1616,17,19,20,22-RP1, LN2-5cm	0.4187	0.0168	-25.16	10.562	126.744	7	6990	330
DB1599-2, LN2-5cm	0.4945	0.0116	-25.99	6.079	72.948	1	5660	190
DB1599-3, LN2-5cm	0.2632	0.0077	-23.95	7.077	84.924	1	10720	240
DB1599-4, LN2-5cm	0.1001	0.0060	-24.74	9.123	109.476	1	18490	490
DB1599-5, LN2-5cm	0.0809	0.0046		11.76	141.12	1	20200	460
DB160-0,1,3,4,5,6,7,8,9 RP1, LN2-39cm	0.2455	0.0245	-27.33	9.583	114.996	9	11280	810
DB1600-2, LN2-39cm	0.1770	0.0050	-29.45	10.952	131.424	1	13910	230
DB1600-3, LN2-39cm	0.0238	0.0035	-28.15	17.004	204.048	1	30010	1170
DB1600-4, LN2-39cm	0.0133	0.0023	-27.15	31.398	376.776	1	34700	1420
DB1600-5, LN2-39cm	0.0105	0.0025	-26.46	26.912	322.944	1	36620	1920
DB1595,1611,12,14,39-RP1, LN2-193cm	0.3827	0.0125	-30.77	10.231	122.772	5	7720	270
DB1639-2, LN2-193cm	0.2206	0.0032	-28.8	19.444	233.328	1	12140	120
DB1639-3, LN2-193cm	0.0549	0.0038	-26.92	14.672	176.064	1	23310	570
DB1639-4, LN2-193cm	0.0244	0.0022	-25.99	33.087	397.044	1	29810	730
DB1639-5, LN2-193cm	0.0192	0.0031	-24.55	19.852	238.224	1	31740	1290
DB1598, 1625, 1626-RP1, LN2-275cm	0.4784	0.0080	-27.97	10.672	128.064	3	5920	140
DB1598, 1625, 1626-RP2, LN2-275cm	0.1334	0.0095	-25.61	8.22	98.64	3	16180	580
DB1598, 1625, 1626-RP3, LN2-275cm	0.0806	0.0099	-27.35	8.099	97.188	3	20220	990
DB1633-1, VC331-43cm	0.2489	0.0049	-24.21	11.242	134.904	1	11170	160
DB1633-2, VC331-43cm	0.1785	0.0038	-23.3	14.73	176.76	1	13840	170
DB1633-3, VC331-43cm	0.0423	0.0024	-23.61	27.498	329.976	1	25400	470
DB1633-4, VC331-43cm	0.0431	0.0022	-23.84	32.549	390.588	1	25250	420
DB1633-5, VC331-43cm	0.0114	0.0023	-22.81	30.042	360.504	1	35910	1650
DB1634-1, VC331-62cm	0.1677	0.0049	-26.62	11.022	132.264	1	14340	240
DB1634-2, VC331-62cm	0.0373	0.0034	-25.08	17.185	206.22	1	26410	740
DB1634-3, VC331-62cm	0.0093	0.0022	-24.36	33.573	402.876	1	37600	1910
DB1634-4, VC331-62cm	0.0077	0.0024	-24.58	29.327	351.924	1	39110	2490
DB1634-5, VC331-62cm	0.0029	0.0021	-23.6	37.608	451.296	1	47020	5830
DB1651-1, VC331-369cm	0.1369	0.0089	-29.39	14.362	172.344	1	15970	530
DB1651-2, VC331-369cm	0.0629	0.0050	-27.15	10.897	130.764	1	22220	640
DB1651-3, VC331-369cm	0.0123	0.0018	-25.82	51.682	620.184	1	35320	1200
DB1651-4, VC331-369cm	0.0071	0.0017	-25.7	100.636	1207.632	1	39760	1920
DB1651-5, VC331-369cm	0.0026	0.0016	-24.24	103.061	1236.732	1	47860	4950

Table DR3